Macromolecules

Article

Cite This: Macromolecules 2018, 51, 4012−4022

Evolution of Nested Folding States in Compression of a Strongly Confined Semiflexible Chain

Simon Bernier,[†] Aiqun Huang,[‡] Walter Reisner,*[,†] and Aniket Bhattacharya*[,‡]

[†]Department of Physics, McGill University, 3600 rue university, Montreal, Quebec H3A 2T8, Canada

[‡]Department of Physics, University of Central Florida, 4111 Libra Drive, Orlando, Florida 32816, United States

Supporting Information

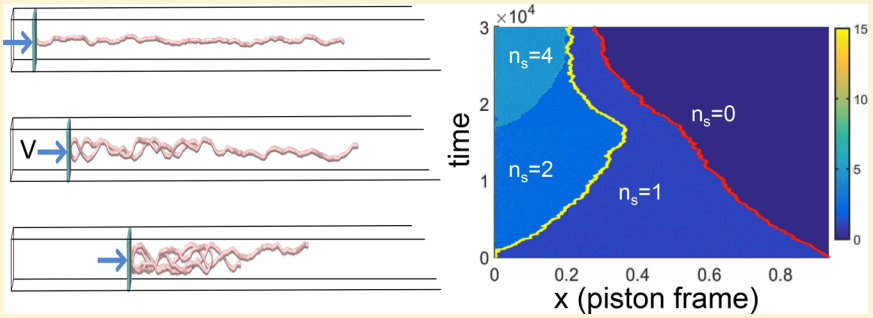

ABSTRACT: We use Brownian dynamics (BD) simulations to probe the physics of nonequilibrium polymer compression in extreme nanoconfinement. In our system, modeled on the "nanodozer assay", a gasket translating at a fixed sliding speed impinges on a nanochannel extended chain. In square channels with diameter much smaller than the chain persistence length, we find that chain compression proceeds through a unique folding kinetics driven by repeated double-fold nucleation events and growth of nested folds. We show that the folding kinetics can be understood by coupling a theory for deterministic contour spooling across the folds with a dynamically varying energy landscape for fold nucleation. These findings are critical for understanding compression of nanochannel confined DNA in the sub-persistence length (Odijk) regime.

INTRODUCTION

Organized states in single macromolecular systems can arise through highly nonequilibrium processes taking place in strongly confined environments. One example of nonequilibrium organization in a confined polymer system occurs during DNA packaging in phages. Powerful motor proteins spool DNA into the capsid, giving rise to an organized state consisting of coaxial spooling about the DNA injection axis.[1,2] An intriguing question is whether such organized nonequilibrium states are specific to active ATP-burning processes in biology or could arise as well in a purely physical process such as mechanical compression or driven transport.[3,4]

Nanochannels serve as an ideal model to study organizing processes in confined environments due to their simplicity, well-characterized equilibrium polymer physics, and usefulness as an experimental platform for resolving dynamic changes in polymer conformation along an effectively one-dimensional spatial axis.[5] When a semiflexible chain is confined in a "nanochannel" with a width D below its persistence length P, back-folding will be suppressed and the chain will extend to almost its full contour length L.[5] Yet, applying a sufficiently high compressive force will drive the nanochannel extended chain into a compressed configuration. For example, in a recent experiment, a translating optically trapped bead was used to dynamically compress a single nanochannel confined DNA molecule.[6,7] Regarding this specific scenario, we can ask: what conditions facilitate emergence of highly organized conformations during chain compression, and how might organization emerge? What role does confinement play? In weak confinement, e.g., to scales much larger than P at which the experiments took place, the compressed chain exists in a disordered blob-melt configuration, analogous to semidilute solution,[8,9] and organization does not occur. Yet, there is no understanding of the compression process at confinement scales $\sim P$ and below: might chain organization be facilitated in these high confinement regimes? In addition, recent single-molecule experiments in the phage system[10] suggest transient nonequilibrium states in DNA packaging can form leading to jamming:[11] is the compaction process smooth, or can jamming occur? Lastly, might dynamical intermediates arise during compression, such as "racket states" observed in simulations of chemical condensation of semiflexible chains in bulk?[12,13] Such questions are not only of theoretical interest: nanofluidic devices can be produced with sub-persistence length dimensions and are routinely used for high throughput mapping applications.[14] Understanding chain compression in such devices is important for understanding how fabrication defects alter chain conformation and distort barcodes. Under-

Received: December 28, 2017
Revised: April 25, 2018
Published: May 17, 2018

DOI: 10.1021/acs.macromol.7b02748
Macromolecules 2018, 51, 4012−4022

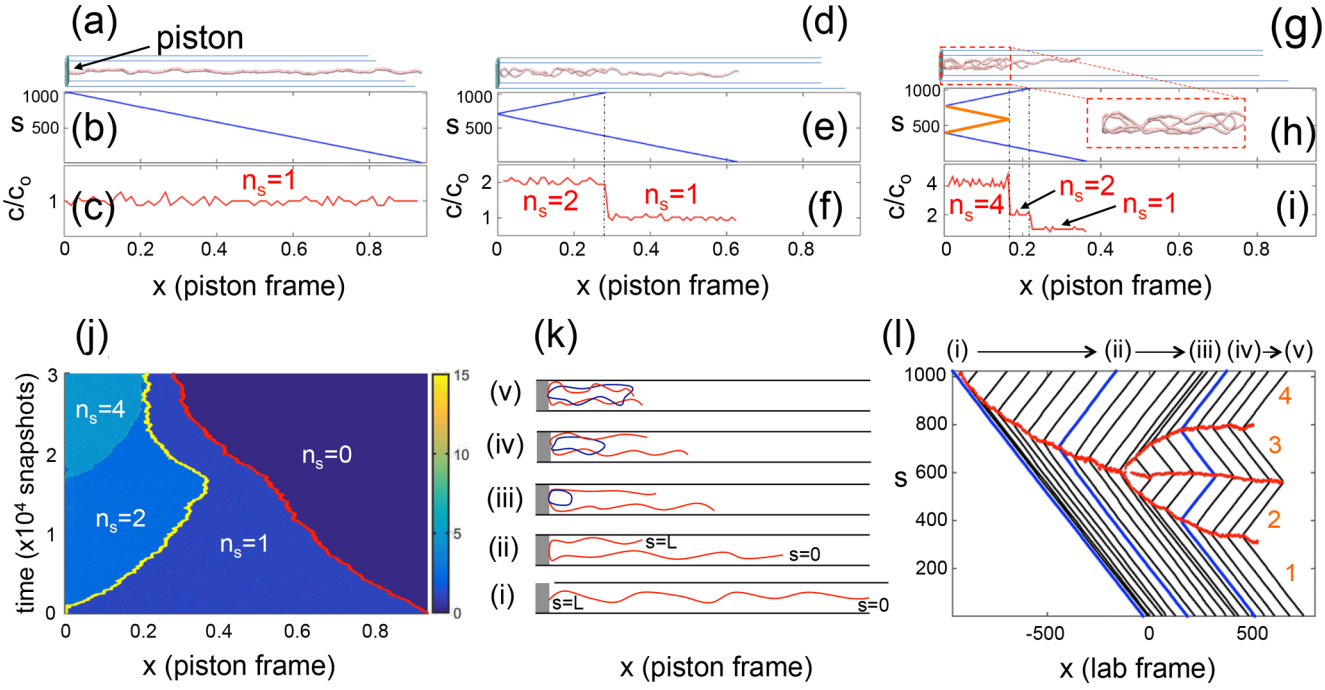

Figure 1. (a) Confined 3D chain profile prior to fold formation (t = 1); (b) corresponding plot of position along chain contour (s) versus position along channel axis (x) and (c) density plot (shown in frame comoving with piston). (d) Chain profile with single-fold (n_f = 1, t = 10 502); (e) corresponding s−x plot shows a kink at the fold location s = 700 and (f) the density profile shows a step between the folded double strand (n_s = 2) and unfolded single-strand (n_s = 1) regions. (g)−(i) same as in (d)−(f) but show formation of a loop structure (n_f = 3, t = 22 502). The two central line segments in (h), colored orange, indicate the contour belonging to the internal loop. (j) The kymograph shows chain coarse-grained concentration, expressed as a color scale, plotted versus x and time. The kymograph shows the intermediate time evolution from (c) → (f) → (i) with the red and yellow curves respectively indicating chain ends at s = 0 and s = L (L = 1024 is total chain contour). (k) Cartoon showing folding structure of chain across the compression event ((i) → (ii) → (iii) → (iv) → (v)). The internal loop, created by double-fold nucleation, is colored purple; note the process of loop inflation from (iii) → (iv) → (v). Note that (i) corresponds to the chain configuration for (a−c), (ii) to the chain configuration for (d−f), and (iv) to the chain configuration for (g−i). (l) Plotting s−x curves in the lab frame for different times through the compression event gives characteristic bifurcation of folds and loop inflation at the n_f = 1 → 3 transition. Numerals (i)−(v) indicate s−x curves that correspond to the cartoon configurations shown in (k). Fitted fold position shown in red; blue trajectories correspond exactly to (b), (e), and (h). The parameters used are D/P = 0.16 (κ = 120) and V = 0.05 (bond-length/snapshot units).

standing chain compression is also critical for characterizing the effect of funneling entrance structures and barrier crossing.[15] For example, in order to generalize the approach developed by Zhou et al.[15] to sub-persistence channels, it is critical to have an underlying understanding of the compression process appropriate for this regime.

We address these questions via a BD implementation of the dynamic compression assay on a model coarse-grained polymeric system.[16] In our system a sliding gasket with fixed speed V translates along a channel of diameter D. As $D < P$ high bending energy suppresses folds in the equilibrium chain configuration leading, for chains of the size simulated, to a complete absence of folding and an equilibrium chain extent r_0 determined entirely by Odijk deflection with the walls. Note that our P value is much lower than that used by Hayase et al.,[17] who set $P \sim L$ (more closely resembling actin than DNA), so our simulation probes a very different confinement regime. We find that chain compression and the emergence of an organized compressed state is linked to the nucleation of hairpin folds (see Figure 1). While "hairpin gas" approaches initially developed in the study of nematics[18] have been used to model the physics of the transition regime in nanochannel confinement[19,20] and model DNA stretching in AC fields,[21] these approaches have focused on thermal generation of folds rather than their generation under compressive forcing. We find that when V is very low, the chain translates along the channel at an extension r only slightly reduced from r_0 (Figure 1a−c). Note that when comparing the chain configuration at different times, it is often convenient to show results in the frame comoving with the piston ("piston frame"), obtained from the "lab frame" (where the channel is at rest) by subtracting off the piston position from the lab frame coordinates (e.g., $x_{piston} = x_{lab} - Vt$). At higher V, hairpin folds nucleate, initially via a single-fold at the piston position (Figure 1d−f), followed by double-folds (Figure 1g−i) that successively emerge at the positions of previous folds. To determine the number of folds n_f on a chain, for a given simulation unit (bead), we plot the bead position along the chain contour (s) versus bead position along the channel (x, see Figure 1b,e,h). Folds appear as V-shaped kinks in such a s−x representation with the V's aligned horizontally (for Figure 1b, n_f = 0 (no folds); for Figure 1e, n_f = 1; and for Figure 1h, n_f = 3). Double-folding gives rise to two oppositely oriented folds that form a loop structure (Figure 1g,h, inset); the strands forming a loop in Figure 1h are colored orange, and a cartoon configuration showing the loop is given in Figure 1k(iv). Note that this structure is called an "S-loop" in the terminology of Dai et al.[20] Every double-fold introduced in the chain gives rise to a loop so a chain with n_f folds has $(n_f - 1)/2$ nested loops. The type of folding observed here is distinct from folding introduced by DNA collision with obstacles under electrophoretic driving,[22−24] or unraveling of hairpin folds due to elongational flows,[25,26] as these classic cases typically involve

DOI: 10.1021/acs.macromol.7b02748
Macromolecules 2018, 51, 4012−4022

dynamics relating to only one fold, but in our system confinement and application of compressive forcing leads to dynamics involving many folds (e.g., $n_f = 3$ in this case, but increasing V can lead to $n_f > 10$).

To connect with experiments performed using DNA molecules with a uniform fluorescent staining, we can extract the local *coarse-grained chain concentration* $c(x,t)$ from the simulation by counting beads that fall within a small predefined bin size of each position. Folds create jumps in $c(x,t)$ leading to corresponding steps in fluorescence along the channel (Figure 1f,i). Such steps could be potentially detected in a manner analogous to classic experiments probing entropically driven chain unfolding in nanochannels.[27] The concentration (or fluorescence) of a local region of channel confined folded polymer is proportional to the number of polymer strands present in that region ($n_s(x,t)$, see Figure 1c,f,i), so we expect the concentration to be roughly quantized in units of the single-strand concentration (c_0). The number of strands in a given section of channel can be determined by counting the number of line segments corresponding to that region in a $s-x$ plot. Note that while $n_s(x,t)$ is integer valued, it a function of position (Figure 1f,i). The *largest* n_s value on a chain, $n_s^{max} = \mathrm{Max}(n_s(x,t))$, is equivalent to the total number of line segments (strands) connecting the fold positions (e.g., for Figure 1e,f $n_s^{max} = 2$ and the configuration contains a single-fold flanked by two strands; for Figure 1h,i $n_s^{max} = 4$ and the configuration contains three folds connected by four strands). Note that $n_s^{max} = n_f + 1$. The position of the concentration steps and their number evolves dynamically during a compression event (Figure 1c,f,i), creating a clear experimental signature of organized folding.

In this article we explore this organized folding process using our BD approach to vary V and P. We also develop a preliminary model to explain our simulation findings in the high stiffness regime. We find that fold nucleation, which gives rise to transitions between states with different n_f values, is determined by the competition between the compression force and the bending energy for forming a fold. We also explore the kinetic problem of how contour is "spooled" from regions of the chain with one polymer strand present ($n_s = 1$) to folded regions ($n_s > 1$). When a chain has just a single-fold, this spooling process is the *reverse* of the classic unfolding problem studied by Levy et al.[27] (e.g., we observe the folding process in the presence of driving forces; Levy et al. observed entropically driven unfolding in the absence of a driving force). For chains possessing a single loop ($n_f = 3$), the contour spools in such a way as to inflate the loop (see Figure 1k). We find that folding kinetics following fold nucleation, including the process of loop inflation, is described by a simple model whereby forces acting across each fold are balanced by friction arising from the cycling contour. Finally, we combine our models for fold nucleation and folding kinetics to describe the predicted average times for nucleation of n_f folds on a chain.

MODEL AND BD SIMULATION DETAILS

Our BD scheme is implemented on a bead–spring model[16] of a polymer with the monomers interacting via excluded volume (EV), a finite extension nonlinear elastic (FENE) spring potential, and a bond-bending potential enabling variation of P (Figure 2). The model, originally introduced for a fully flexible chain by Grest and Kremer,[28] has been studied quite extensively by many groups using both Monte Carlo (MC) and various molecular dynamics (MD) methods.[29] Recently, we have generalized the model for a semiflexible chain and studied

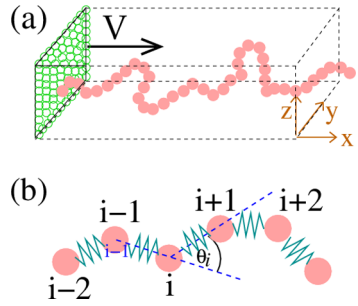

Figure 2. Model system on which BD simulation is performed. (a) A confined bead–spring chain inside a rectangular nanochannel is pushed by the green piston (nanodozer assay) toward the right at velocity $V = V_{piston}$. The confinement potentials are imposed on four (two xy and two xz) planes and by the moving piston in the yz plane in the positive x direction. The chain is free to move on the side opposite the piston. (b) Schematic showing details of the bead–spring chain parametrization.

both equilibrium and dynamic properties.[30] Comparison of our BD results with those obtained for very large self-avoiding chains on a square lattice reveals robustness of the model for certain universal aspects, e.g., scaling of end-to-end distance and transverse fluctuations.[30,31,32,33] Using our BD scheme for confined stiff polymers in nanochannels, we have demonstrated and verified the existence of Odijk deflection length $\lambda \sim (PD^2)^{1/3}$.[33,34] More recently, we compared the evolution of the density profile along the nanochannel axis obtained from the BD simulation with those obtained from an approach using nonlinear partial differential equation[16] with excellent agreement showing the applicability of the BD simulation method to study nonequilibrium dynamics of confined polymers.

We keep the channel width D and the contour length L fixed but allow P to vary, so as to explore chains of different stiffness subject to different piston velocity V; note V values are quoted in units of bond length/snapshot, with 1 snapshot = 1000 simulation iterations). The EV interaction between any two monomers i and j of diameter σ_b is given by a short-range truncated Lennard-Jones (LJ) potential U_{LJ} (eq 1) of strength ϵ given by

$$U_{LJ} = 4\epsilon \sum_{i<j}^{N} \left[\left(\frac{\sigma_b}{r_{ij}} \right)^{12} - \left(\frac{\sigma_b}{r_{ij}} \right)^{6} \right] + \epsilon \quad \text{for } r_{ij} \le 2^{1/6}\sigma_b$$
$$= 0 \quad \text{for } r_{ij} > 2^{1/6}\sigma_b \tag{1}$$

where $r_{ij} = |\vec{r}_i - \vec{r}_j|$ is the distance between any pair of beads. The successive monomers are connected by a finite extension nonlinear elastic (FENE) spring potential (eq 2)

$$U_{FENE} = -\frac{1}{2} k_{FENE} {R_0}^2 \sum_{i}^{N-1} \ln(1 - {r_{i,i+1}}^2/{R_0}^2) \tag{2}$$

where k_{FENE} is the spring constant and R_0 is the allowed maximum bond length. The parameters k_{FENE} and R_0 along with ϵ and σ_b determine the bond length. The chain stiffness is controlled by a three body bond-bending potential

$$U_{bend} = \kappa \sum_{i=2}^{N-1} (1 - \cos\theta_i) \tag{3}$$

DOI: 10.1021/acs.macromol.7b02748
Macromolecules 2018, 51, 4012–4022

Here $\theta_i = \cos^{-1}\left(\frac{\vec{b}_{i-1}\cdot\vec{b}_i}{|\vec{b}_{i-1}||\vec{b}_i|}\right)$ is the angle between two successive bond vectors $\vec{b}_{i-1} = \vec{r}_i - \vec{r}_{i-1}$ and $\vec{b}_i = \vec{r}_{i+1} - \vec{r}_i$, respectively, as shown in Figure 2b. In three dimensions, for $\kappa \neq 0$, the persistence length P of the chain is related to κ via[35]

$$P = \frac{\kappa\sigma_b}{k_B T} \tag{4}$$

where k_B is the Boltzmann constant and T is the temperature.

The confining walls and the piston (shown in green) consist of equally spaced LJ particles of the same diameter σ_b and the same repulsive interaction ϵ. While the wall particles are immobile, the relative positions of the piston particles are fixed, and all of them together advance a certain distance at the end of every BD step toward right (x direction, see Figure 2a) to push the polymer beads forward. The length and energy are measured in units of σ_b and ϵ. The time is measured in units of $\sqrt{m\sigma_b^2}/\epsilon$, where the mass m is typically the mass of a nucleotide. We chose the width $D/\sigma_b = 16$ and the chain length $L/\sigma_b = N = 1024$ and varied the chain stiffness κ from 2 to 120 to cover a wide range of D/P and L/P and studied the compression process for several different values of V.

We use the following Langevin dynamics equation of motion to advance the position of the ith monomer

$$m\ddot{\mathbf{r}}_i = -\nabla(U_{LJ} + U_{FENE} + U_{bend} + U_{wall} + U_{piston}) - \gamma\mathbf{v}_i + \mathbf{W}_i \tag{5}$$

where γ is the monomer friction coefficient, and $\mathbf{W}_i$ is a Gaussian random force with zero mean at temperature T, and satisfies the fluctuation−dissipation relation $\langle \mathbf{W}_i(t)\cdot\mathbf{W}_j(t')\rangle = 2dk_BT\gamma\delta_{ij}\delta(t-t')$ in d dimensions ($d = 3$ in this case), δ_{ij} is the Kronecker delta ($\delta_{ij} = 0$ for $i \neq j$ and $= 1$ for $i = j$), and $\delta(t-t')$ is the Dirac delta function. Note that hydrodynamic interactions are not included in our approach. For channels in the Odijk regime we expect that the friction factor of a confined single-strand is proportional to the contour length,[36] with the effect of hydrodynamic interactions simply to renormalize the friction prefactor. The question of how hydrodynamic interactions alter coiled regions with $n_s > 1$ is more subtle, as the kinetics in this case involves organized self-reptation of the chain through the folding network created by compression, creating a situation where adjacent strands slide in opposite directions (quite distinct from problems involving the motion of the polymer coil as a whole). Similar problems arise in analyzing the effect of hydrodynamic interactions on knot diffusion by self-reptation along an extended chain. Knot diffusion studies find that hydrodynamic interactions have only a moderate, purely quantitative effect on the knot diffusion constant, altering the diffusion constant by about a factor of 1.5 but not altering the scaling of the knot diffusion constant with knot length.[37] We thus expect that the effect of hydrodynamic interactions will be simply to renormalize the friction factor γ.

The numerical integration of eq 5 is implemented using the algorithm introduced by Gunsteren and Berendsen.[38] Our previous experiences with BD simulation suggests that appropriate parameter specifications are $\gamma = 0.7$, $k = 30$, $R_0 = 1.5$, and the temperature $k_BT = 1.2$. For a time step $\Delta t = 0.01$ these parameter values produce stable trajectories over a very long period of time and do not lead to unphysical crossing of a bond by a monomer.[32,33] The average bond length stabilizes at $b_l = 0.97 \pm 0.002$ with negligible fluctuation regardless of the chain size and rigidity.[32] The piston velocity is adjusted by moving the piston by a distance 10^{-5}−10^{-4} in units of σ_b at the end of every BD step, and we store chain configurations typically every 1000 time steps. In our analyses we use the 1000 frames/snapshot as the reduced unit to report our results.

Initially a chain in linear configuration is placed inside the nanochannel and allowed to equilibrate with equilibrium time much longer than the relaxation time ($\tau_{eq} \sim N^{1+2\nu}$, where $\nu = 0.59$ is the Flory exponent in 3D). Then the piston is placed next to the first bead and the pushing phase starts. The BD simulation time for the pushing phase is decided by ensuring that the whole chain is in a steady state after getting compressed. The BD simulation time can be prohibitively large for low velocities and for stiffer chains. For each κ and V, the density profile $c(x,t)$ is averaged over ten independent runs. The total calculation time is approximately equivalent to running the code continuously for about 6 months on a 10 processor Intel Pentium quad-core cluster.

SIMULATION RESULTS

In order to efficiently visualize the chain conformation throughout the compression process, we introduce two representations: a *kymograph* representation (Figure 1j) to display the time evolution of chain concentration and a *folding plot* representation (Figure 1l) to indicate the dynamics of the chain's global folding structure. Figure 1k gives a series of cartoon chain configurations that follow the folding process displayed in Figure 1j,l. Configuration i corresponds to the chain state in Figure 1a−c, configuration ii corresponds to the chain state in Figure 1d−f, and configuration iv corresponds to the chain state in Figure 1g−i. In the kymograph (Figure 1j), color corresponds to chain concentration and is plotted as a function of time and position (in the piston frame). The x positions of the chain edges are also indicated (yellow corresponds to chain edge at $s = L$, with $L = 1024$ the chain contour length; red corresponds to chain edge at $s = 0$). The transfer of contour from regions with a single-strand present ($n_s = 1$) to regions with multiple adjacent strands is evident as the compression proceeds. Transfer initially occurs from the single- to two-stranded region (Figure 1k, configuration ii); then at around $t = 1.75 \times 10^4$ a four-strand ($n_s = 4$) region is formed and grows at the expense of the single- and two-stranded region, corresponding to the creation of a loop (Figure 1k, configuration iii−iv). The final chain state is almost completely composed of a $n_s = 4$ region (Figure 1k, configuration v).

In a folding plot (Figure 1l), we show s−x curves for different time points. These plots are shown in the lab frame to ensure that each s−x curve can be clearly distinguished (as the piston pushes the chain, the chain configuration gets translated in the lab frame, ensuring separation between the s−x curves). We also indicate the position of each fold (red), determined from the s−x plots using an automated peak-detection algorithm (Matlab, "findpeaks"); branching of the fold position curve indicates double-fold formation. As we proceed from left to right in Figure 1l, initially the chain has no-fold (Figure 1k, configuration i), then very quickly a fold nucleates (Figure 1k, configuration ii), and contour spools from the strand (located below the fold position) across the fold, forming a second strand (located above the fold position) that grows in time, driving the fold to lower s values. Then a double-fold nucleates, creating a bifurcation fork in the fold position plot. The resulting loop structure grows or "inflates" as the two strands flanking the central fold (strands 2 and 3) increase in length, and the strands at the chain edges (strands 1 and 4) decrease in

DOI: 10.1021/acs.macromol.7b02748
Macromolecules 2018, 51, 4012−4022

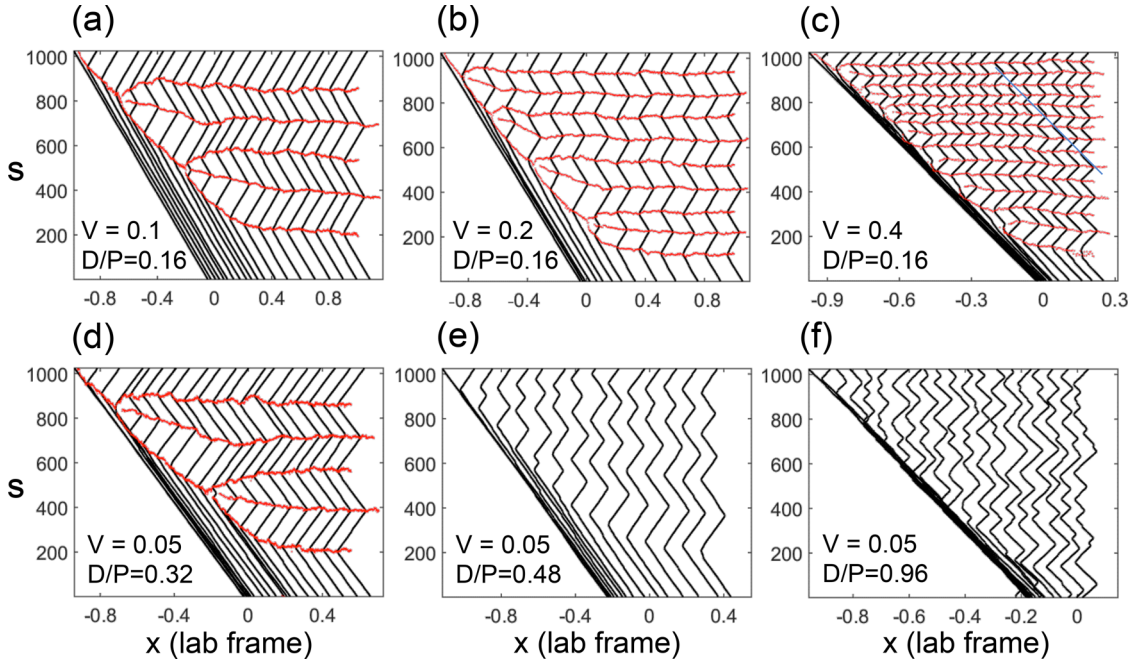

Figure 3. Plots of chain contour s vs x position in lab frame at different times for varying piston speed V (a–c) and chain stiffness (d–f). The compression process proceeds from left to right. The fitted fold positions are shown in red. Note that (a) corresponds to an event with $n_f = 5$, (b) $n_f = 9$, (c) $n_f = 15$, (d) $n_f = 5$, and (e) $n_f = 7$. The piston velocity is in units of bond length/snapshot. We show examples of concentration kymographs and raw chain configurations corresponding to these compression events in the Supporting Information (Figures S1 and S2).

length. This is equivalent to the formation of the $n_s = 4$ region in the kymograph. The loop grows until it extends across almost the entire chain (Figure 1k, configurations iii–v). Dynamic evolution of the chain conformation halts when each of the four strands are roughly equal, leading to a chain with $n_f = 3$ almost completely in a $n_s = 4$ state. We do not observe any departure from this steady-state configuration over a total runtime about 3 times longer than shown (see Figure S1 in Supporting Information).

Figure 1 shows typical compression behavior in the limit of high chain stiffness at moderate piston velocity ($D/P = 0.16$; $V = 0.05$). Figure 3a–c shows additional examples of compression events for chains of the same stiffness for increasing V (example concentration profiles, real chain configurations, and kymographs corresponding to these events are shown in Figures S2 and S3). Evidently, the number of folds increases with increasing piston velocity (we have observed folding numbers up to $n_f = 15$, for Figure 3c). For these events the nucleation and inflation dynamics proceeds in a remarkably regular fashion. A single-fold and then double-fold nucleate in sequence (Figures 1l and 3a–c) so that n_f is restricted to odd values 0, 1, 3, 5, 7, ... We observe that folds are always nucleated very close to the position of previous folds abutting the piston (Figures 1l and 3a–c). If the number of folds created on the chain exceeds three (e.g., Figure 3a–c), then there will be two or more folds abutting the piston. In this case, the fold will always be nucleated at the fold position lying at lowest s (e.g., closest to the chain end at $s = 0$). Finally, toward the extreme right of the plots, in the long time limit, the length of polymer segments connecting folds becomes roughly equal (Figures 1l and 3a,b), a signature of an organized folding structure consisting of $(n_f - 1)/2$ nested loops of equal size with the "tips" of the hairpin folds closely aligned. Note that the event shown in Figure 3c has not quite reached steady state, although the fold spacing is roughly equal for folds at high s. Decreasing P leads to a breakdown in the regular dynamics and a growing disorder of the global folding state (Figure 3d–f). The regular dynamics and organized folding is evident down to $D/P = 0.48$ (Figure 3e, although note greater fluctuation in length of connecting segments). For $D/P = 0.96$ (Figure 3f), the dynamics and folding structures become highly disordered as the edge of the Odijk regime is reached. Folding is still evident, but connecting polymer segments between folds fluctuate greatly in length and the dynamics no longer corresponds to a regular sequence of folding events, with folds formed at random positions and times.

DOUBLE-FOLD NUCLEATION

A key question is the physics determining the fold nucleation process and loop inflation dynamics that facilitate the regular folding dynamics and organized folding structure observed for $D/P < 0.5$ (Figures 1l and 3a–c). This behavior is unique to the Odijk regime and is dramatically different from the compression physics observed for $D/P > 1$, which consists of a packing of disordered blobs.[16] A key problem in understanding this dynamics is determining why the folds appear at the times they do for a given chain stiffness and piston velocity. Answering this question requires addressing two distinct physical problems: (1) the free energy landscape of fold nucleation, which determines the energetic barrier for forming a fold (explored in the section Double-Fold Nucleation), and (2) the kinetics driving the motion of the fold positions once they are formed (explored in the section Fold Dynamics). Once solved, these problems can be combined to determine the average times at which folds are formed (see section Dynamic Compressive Force and Fold Nucleation Times).

The compression is most conveniently modeled in the frame of reference moving with the piston. In this frame, the chain is compressed against a fixed barrier gasket in a uniform flow of speed V, generating a "flow force" on a segment of contour l

DOI: 10.1021/acs.macromol.7b02748
Macromolecules 2018, 51, 4012–4022

given by $f_l = \gamma V l$. In order to model fold nucleation, we focus on the detailed chain configuration at the piston for time-points straddling a folding transition. For a transition from zero to one fold (e.g., $n_f = 0 \rightarrow 1$, Figure 4a), we observe that the single

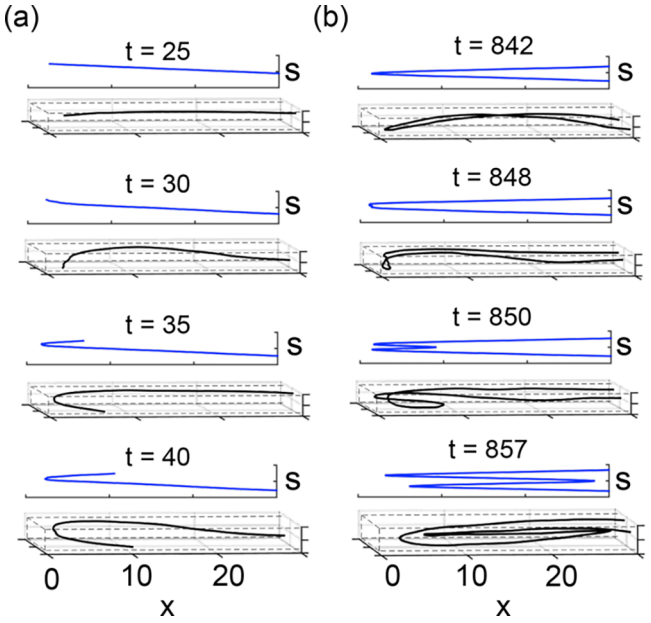

Figure 4. (a) Chain configuration for frames straddling nucleation of a single-fold event with $D/P = 0.16$ ($\kappa = 120$) and $V = 0.05$ (blue curve: $s-x$ plot; black curve: 3D chain configuration). (b) Chain configuration for frames straddling nucleation of a double-fold event with $D/P = 0.16$ ($\kappa = 120$) and $V = 0.05$ (blue curve: $s-x$ plot; black curve: 3D chain configuration).

strand will fluctuate from an extended conformation to a conformation bent at the gasket; a single-fold will nucleate when the bending angle exceeds 180°. For higher order transitions involving double-fold formation (Figure 4b), we observe that just prior to the transition the single-fold will buckle and bend upward forming a "hinged state"; a double-fold will nucleate if the hinge can rotate through 180°. We choose to focus on double-fold formation, the process key for understanding the higher order transitions that drive formation of large n_f states.

The free energy barrier to nucleate folds decreases as the piston velocity increases. In order to quantify this effect, we determine the free energy of the hinge state as a function of bending angle θ (see Figure 5a,b for geometry of the hinge state and definition of θ). We hypothesize that the free energy barrier F_b exists at a critical $\theta_b \leq 180°$: once $\theta > \theta_b$ the hinge can proceed through 180° leading to nucleation of a double-fold. Determining F_b exactly is challenging as we would need to estimate the free energy contribution of the ensemble of possible hinge trajectories consistent with a particular angle θ and the geometric constraints imposed by the channel. A rigorous treatment might find the confined chain configuration under compressive force that minimizes the wormlike chain bending energy[39] or use an exact Green's function solution.[40] Our objective here is to develop a simplified model that can semiquantitatively capture simulation trends. We neglect fluctuations and crudely parametrize a "hinge state" at the end of two segments (see Figure 5a,b) as being formed from two parallel circular arcs (contour L_c, angle θ, lying in $x-z$ plane), connected to straight segments (contour L_s), that are

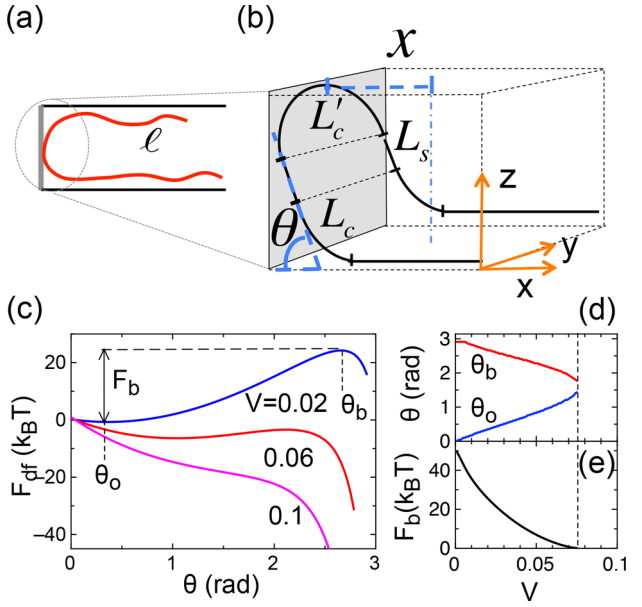

Figure 5. (a) Schematic showing chain configuration with single bend; l is the contour of the shortest strand flanking the fold. (b) Schematic showing detailed parametrization of "hinge state" formed upon compression of chain against piston. The hinge is constructed from (1) two parallel circular arcs of contour L_c, sweeping through an angle θ, giving the overall hinge rotation; (2) the arcs connect to two straight segments of contour L_s, rotated by angle θ with respect to the x-axis; (3) the straight segments are joined by a single half-circular arc of contour L_c'. (c) Double-fold free energy F_{df} versus θ. The free energy barrier F_b is shown for $V = 0.02$. (d) Hinge rotation at barrier (θ_b) and hinge rotation of the metastable intermediate configuration (θ_0) versus V. (e) The free energy barrier for double-fold nucleation F_b versus V. The dashed line indicates critical velocity where barrier vanishes. Curves shown are obtained for $l = L/2$.

then bridged by a third arc (contour L_c', angle π) with a cord perpendicular to the adjoining line segments (the detailed parametrization is given in the Supporting Information). The free energy for forming the hinged state includes contributions from the bending energy of the arcs and the flow-work $W(\theta,l)$:

$$F_{df} = \frac{P\theta^2}{L_c} + \frac{P\pi^2}{2L_c'} + W(\theta, l) \tag{6}$$

If the total contour in the hinge region is small compared to the contour of the strand (e.g., $L_0 \ll l$), then the compressive force f_l acting on the hinge state will be independent of the hinge angle and the flow work $W(\theta,l) = \int_0^{\delta x} f_l(\theta')\, dx = f_l \delta x$. The quantity δx is the change in strand extent due to hinge formation (note that $\delta x < 0$ as the strand extent decreases when the hinge is formed). In particular, $\delta x = -L_0/2 + x_f(L_0)$, where $x_f(L_0)$ is the x-extent of the hinged region and $-L_0/2$ is the decrease in extent of the nonhinged region assuming contour is withdrawn symmetrically from both strands into the hinge. In general, f_l is not constant but decreases when the hinge region is formed as contour is removed from the strand and oriented perpendicular to the flow (we provide a detailed estimate of this effect in the Supporting Information).

In order to evaluate the free energy as a function of θ, we need to determine the contour of each segment of the hinge (L_c, L_c', and L_s). The free energy is minimized when the perpendicular arc, aligned along y, expands to minimize bending energy and the bend tip, to maximize flow work, is

DOI: 10.1021/acs.macromol.7b02748
Macromolecules 2018, 51, 4012−4022

forced against the wall (maximizing hinge z extent). These two constraints fix L_c and L_c'; we find L_s by minimizing F_{df}. The resulting free energy profile $F_{df}(\theta)$ determines the landscape for double-fold nucleation (Figure 5c). Note that in this plot we cut off the profile when L_s reaches the Odijk deflection length $\lambda = (PD^2)^{1/3}$, as beyond this point fluctuations cannot be neglected (note that the free energy maximum arises for $L_s < \lambda$). As hypothesized, the free energy landscape does possess a free energy barrier F_b for nucleation at a critical θ_b. For low V the hinge energy also has a local minimum at θ_0. When V is low, the nucleation barrier F_b is high, θ_b is large, and θ_0 is close to zero (Figure 5d,e). Increasing V increases $\theta_0 > 0$: this is indicative of a hinged intermediate state, i.e., a configuration which is slightly bent under compressive forcing. The barrier is still present but is reduced by flow work and can be crossed via Kramer's escape.[4] At even higher V the barrier disappears entirely. This approach applies directly to a $n_f = 1 \rightarrow 3$ transition but can be extended to higher transitions, neglecting excluded-volume interactions between multiple piston localized folds.

FOLD DYNAMICS

Once a fold or double-fold is nucleated, the chain will be in an unstable configuration due to an imbalance of flow forces acting on the strands flanking the fold position(s). Contour will spool across the fold position(s) from the long flanking strand into the shorter flanking strand. This spooling process will cause the fold position(s) to migrate along the chain contour (Figure 6). After nucleation of a single-fold, the fold position will move from the $s = 0$ position toward $s = L/2$ (Figure 6a–c), following a kinetics which is the "reverse" of entropic unfolding.[27] After double-fold nucleation, a more complex folding dynamics arises (Figures 1k and 6d–f), involving contour spooling from segments on the chain edges (L_1, L_4) to inflate the internal loop (L_2, L_3). After nucleation of a second double-fold (Figure 6g–i), contour spools from the initial loop (L_4, L_5) and strands on the chain edges (L_1, L_6) into the second loop (L_2, L_3). Note that in complex scenarios involving dynamics of multiple folds, only fold positions neighboring the growing loop in contour show a high degree of dynamics (e.g., in Figure 6h,i fold position s_5 hardly moves at all, s_4 shows a little dynamics, and s_1, s_2, and s_3 are highly dynamic).

We can develop a simple kinetic model to describe the spooling process. To describe kinetics following a $n_f = 0 \rightarrow 1$ transition, we divide the chain into segments of size L_1 and $L_2 = L - L_1$ (Figure 6a). The "spooling force" f_s driving contour from segment L_1 to L_2 is $f_s = \gamma V(L_1 - L_2)$, balanced by a drag force $f_d = \xi(dL_1/dt)$, with the friction factor $\xi = \gamma L$ determined by spooling contour from one chain end to another across the fold position. In principle, entropic forces would resist spooling,[27,41] but we find that these are small and not required to describe the simulation results. This kinetic framework leads to an equation for $L_1(t)$:

$$\frac{dL_1}{dt} = -V\frac{L_1 - L_2}{L} = -V\frac{2L_1 - L}{L} \quad (7)$$

The time dependence of the fold position in contour space, $s_1 = L_1$, is then determined by the simple-exponential relaxation:

$$s_1(t) = (L/2)(1 + \exp(-t/\tau)) \quad (8)$$

with the relaxation time scale $\tau = L/2V$. Two examples of single-fold kinetics are shown in Figure 6b,c; the simple kinetic model describes simulation very well. When plotted versus rescaled time t/τ, the single-fold time evolution for simulations with different stiffness and V collapse onto a master curve well described by eq 8 (see Figure 7).

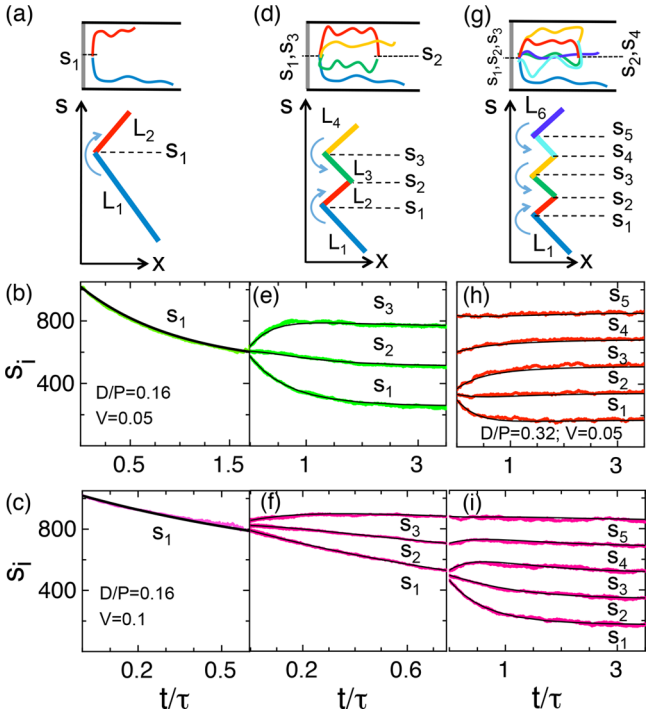

Figure 6. (a) Cartoon configuration and s–x plot, giving direction of contour spooling, for state with single-fold at contour position s_1. Example of spooling dynamics after formation of a single-fold for compression event with (b) $D/P = 0.16$ ($\kappa = 120$); $V = 0.05$ and (c) $D/P = 0.16$ ($\kappa = 120$); $V = 0.1$. The green and magenta curves are simulation; black curve is prediction of kinetic model (note excellent agreement). (d) Cartoon configuration and s–x plot for state with three folds at contour positions s_1, s_2, and s_3. Example of spooling dynamics after double-fold nucleation, leading to state with three folds, for compression event with (e) $D/P = 0.16$ ($\kappa = 120$) and $V = 0.05$; and (f) $D/P = 0.16$ ($\kappa = 120$) and $V = 0.1$. The green and magenta curves are simulation; black prediction of kinetic model. (g) Cartoon configuration and s–x plot for state with five folds at contour positions s_1, s_2, s_3, s_4, and s_5. Example of spooling dynamics after nucleation of *second* double-fold, leading to a state with five folds, for compression event with (h) $D/P = 0.32$ ($\kappa = 60$) and $V = 0.05$; and (f) $D/P = 0.16$ ($\kappa = 120$) and $V = 0.1$. The red and magenta curves are simulation; black curve is prediction of kinetic model. All simulation curves are averaged over five individual simulation events; one sigma error bars are on order of line thickness. Note that (b)–(e) show the single-fold and then 3-fold kinetics for the same compression event (with $D/P = 0.16$, $V = 0.05$); (c)–(f)–(i) show single-fold, 3-fold, and then 5-fold kinetics for the same compression event (with $D/P = 0.16$, $V = 0.1$).

Using a similar approach, we can describe kinetics following transitions to higher order folding states. Following a $n_f = 1 \rightarrow 3$ transition (Figure 6d), the internal loop corresponds to segments L_2 and L_3, which must be equal. Spooling forces $f_{s1} = \gamma V(L_1 - L_2)$ and $f_{s2} = \gamma V(L_4 - L_3)$ drive contour into L_2 and L_3 across the fold positions s_1 and s_3. The friction factors reflect dissipation arising from contour cycling across the chain portions flaking each fold: $\xi_1 = L_1 + L_2$ and $\xi_2 = L_3 + L_4$. The resulting kinetics is described by

$$\frac{dL_1}{dt} = -V\frac{L_1 - L_2}{L_1 + L_2} \quad \text{and} \quad \frac{dL_4}{dt} = -V\frac{L_4 - L_3}{L_3 + L_4} \quad (9)$$

DOI: 10.1021/acs.macromol.7b02748
Macromolecules 2018, 51, 4012–4022

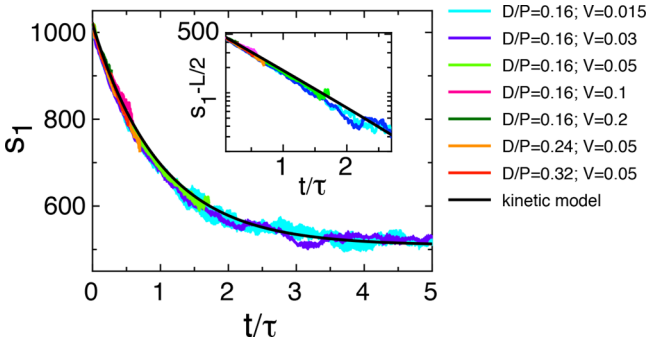

Figure 7. Data collapse for single-fold position versus time. Cyan curve gives simulation results for $D/P = 0.16$ ($\kappa = 120$) and $V = 0.015$; blue gives simulation results for $D/P = 0.16$ ($\kappa = 120$) and $V = 0.03$; light-green gives simulation results for $D/P = 0.16$ ($\kappa = 120$) and $V = 0.05$; pink gives simulation results for $D/P = 0.16$ ($\kappa = 120$) and $V = 0.1$; dark-green gives simulation results for $D/P = 0.16$ ($\kappa = 120$) and $V = 0.2$; orange gives simulation results for $D/P = 0.24$ ($\kappa = 80$) and $V = 0.05$; red gives simulation results for $D/P = 0.32$ ($\kappa = 60$) and $V = 0.05$. The black curve shows kinetic model prediction (eq 8, using $L = 1024$). Error bars, resulting from the standard deviation over the simulation runs for each curve, are on order of the line thickness. Note that the agreement with theory is very good. The inset gives $s - L/2$ versus t/τ on a log−linear scale, which shows linear behavior, as predicted by eq 8.

Equation 9 agrees well with simulation (Figure 6e,f).

We can model even higher transitions; for example, fold position evolution following a $n_f = 3 \rightarrow 5$ transition is shown in Figure 6g. In this case, the new double loop, with fold positions s_2 and s_3, is formed at contour position s_1 in the initial $n_f = 3$ state. We then divide the chain into six segments (L_1 to L_6, see Figure 6g). The contour in each half of an internal loop is equal to the contour of the other half (i.e., $L_2 = L_3$ and $L_4 = L_5$). Contour conservation forces $L = L_1 + 2L_2 + 2L_4 + L_6$. A spooling force $f_{s1} = \gamma V(L_1 - L_2)$ drives contour from segment L_1 to L_2; a spooling force $f_{s2} = \gamma V(L_4 - L_3)$ drives contour from L_4 to L_3 and a spooling force $f_{s3} = \gamma V(L_6 - L_5)$ drives contour from L_6 to L_5. These spooling forces are balanced respectively by drag forces $f_{1d} = \xi_1(dL_1/dt)$ and $f_{2d} = \xi_2(dL_4/dt)$ and $f_{3d} = \xi_3(dL_6/dt)$ with the friction factors $\xi_1 = L_1 + L_2$, $\xi_2 = L_3 + 2L_4 + L_6$, and $\xi_3 = L_3 + 2L_4 + L_6$. Note that the friction factors reflect the length of chain involved in the contour transfer. The transfer of contour from segment L_1 to L_2 involves sliding of the chain segment $L_1 + L_2$; transfer of contour into the growing loop from the other half of the chain (e.g., consisting of segments L_4, L_5, and L_6) involves coordinated motion of all these segments, in addition to the segment L_3 in the growing loop. The resulting kinetics is described by the system

$$\frac{dL_1}{dt} = -V\frac{L_1 - L_2}{L_1 + L_2}$$
$$\frac{dL_4}{dt} = -V\frac{L_4 - L_3}{L_3 + 2L_4 + L_6}$$
$$\frac{dL_6}{dt} = -V\frac{L_6 - L_5}{L_3 + 2L_4 + L_6} \quad (10)$$

with the evolution of the growing loop $2L_2$ obtained from solving the contour conservation relation for L_2. The fold positions are determined from $s_1 = L_1$, $s_2 = L_1 + L_2$, $s_3 = L_1 + 2L_2$, $s_4 = L_1 + 2L_2 + L_4$, and $s_5 = L - L_6$. The result of numerical solution of the system eq 10 is shown in Figure 4h,i against simulation for compression with two different parameter combinations. Again, the agreement with simulation is very good, even for the nontrivial spooling dynamics in configurations with many folds. We can extend the same argument to construct equations describing the evolution of even higher order folding states. The systems of ode's are solved numerically using Matlab's ode23 solver.

DYNAMIC COMPRESSIVE FORCE AND FOLD NUCLEATION TIMES

We can combine the nucleation theory and folding kinetics to predict the specific folding times. We argue that spooling dynamics is sufficiently slow so that l and the compressive force are approximately constant during a transition (e.g., we argue the process is quasi-static). The compressive force driving nucleation grows as the flanking strand lengthens due to spooling (e.g., $l = L_2(t)$, see Figure 5a). The growth of L_2 leads to an increasing compressive force on the chain edge that may eventually nucleate another fold. However, this situation is dynamic, and we need to include viscous forces acting on the strands. In addition, one expects that the strand $L_1(t)$ may also exert compressive forces.

We can resolve these conceptual problems via the following argument. Qualitatively, we do not expect a compressive force to arise in a situation where contour is slipping across s_1 (from L_1 to L_2) with no resistance (e.g., at a rate equal to the flow speed V). This is true for very short times after the nucleation event, where L_2 is close to zero. As L_2 grows, a back-force will be produced that decreases the spooling rate below V; compressive force will now start to grow in strands 1 and 2. The compressive force on the two strands, working in the piston frame, will include the flow-force (e.g., $f_l = \gamma Vl$) and an additional component due to viscous drag arising from spooling of contour along the strands. The quantity $V_s \equiv -dL_1/dt$ gives the rate at which contour is spooling from strand 1 into strand 2, equivalent to the rate at which contour is moving in the piston frame in strand 1 and 2 or the spooling speed in both strands. Equations 7, 9, and 10 each give an identical expression for V_s (i.e., it does not depend upon the number of folds):

$$V_s = V\frac{L_1 - L_2}{L_1 + L_2} \quad (11)$$

Note that while this is a subtle point, dL_2/dt is not equal to V_s as contour can escape from the opposite end of strand 2 into strand 3 (some contour spooling along strand 2 ends up increasing the length of strand 2, but some contour ends up moving into strand 3 instead with the increase in L_2 dictated by overall contour conservation). The viscous drag force acting on strand 1 due to spooling ($f_{d1} = \gamma V_s L_1$), will oppose spooling, and thereby point away from the piston so that the compressive force is reduced in strand 1. The total dynamic compressive force on strand 1 is thus the sum of the flow force and viscous drag:

$$f_{c1} = f_{L_1} - f_{d1} = \gamma L_1(t)(V - V_s) \quad (12)$$

In contrast, the drag force on strand 2 ($f_{d2} = \gamma V_s L_2$) will—in opposing spooling—point toward the piston and thereby act to increase the compressive force on strand 2 so that the total dynamic compressive force is

$$f_{c2} = f_{L_2} + f_{d1} = \gamma L_2(t)(V + V_s) \quad (13)$$

Inserting eq 11 into eq 12 and eq 13 yields

DOI: 10.1021/acs.macromol.7b02748
Macromolecules 2018, 51, 4012−4022

$$f_c \equiv f_{c1} = f_{c2} = 2\gamma V \frac{L_1 L_2}{L_1 + L_2} \tag{14}$$

Equation 14 shows that if we include the viscous forces, the compressive forces acting on both strands are *equal*. At short times, when $L_1 \gg L_2$, eq 14 yields $f_c = 2\gamma V L_2$; at long times, when $L_1 = L_2 = L/(n_f + 1)$, eq 14 yields $f_c = \gamma V L/(n_f + 1)$, recovering the expected long time result when $V_s = 0$.

The quasi-static assumption, eq 6, eq 13, and eq 14 can be used to determine the dynamic free energy barrier $F_b(f_{c2}(t),L_2(t))$ for double-fold nucleation during the spooling process. Kramers theory then gives a time-dependent nucleation rate:

$$R(t) = (1/\tau_0)\exp[-F_b(f_{c2}(t), L_2(t))] \tag{15}$$

with τ_0 is a prefactor with dimensions of time, depending upon the diffusional rotation of the hinge as well as the curvature at the free energy maxima and minima. We assume τ_0 is constant and find it through fitting to simulation data. The probability $P_s(t)$ that a system will survive in the n_i fold state for time t is given by $P_s(t) = -\exp[\int_0^t R(t')\,dt']$. The probability of a nucleation event occurring at time t in interval dt is $P_n(t) = dtR(t)P_s(t)$. The distributions P_n are very sharp (Figure 8a), as nucleation will tend to occur at the time when the compressive force drops the free energy barrier to around k_BT, leading to a well-defined nucleation time $t_{av} = \int P_n(t)t\,dt$.

Figure 8a,b shows, for simulation and theory, t_{av} of observed transitions as a function of n_f (Figure 8b) and of V (Figure 8c). The simulation trends are well captured for $V < 0.4$; in particular, the theory predicts a sharp decrease in t_{av} at a series of critical V's, opening up successively higher folding states as V is increased. This trend is consistent with the increase in n_f observed in simulation as V is increased (Figure 3a–c). Qualitatively, the sharp decrease in transition time arises when the maximum compressive force the chain can exert is sufficient to drop the nucleation barrier to $\sim k_BT$. The theory fails to quantitatively describe higher transitions for $V = 0.4$, likely due to a failure of the quasi-static approximation for such high V.

After the rapid decrease in t_{av}, the transition time curves appear to approximately follow power laws. In particular, the theory curves over an intermediate range of V (see Figure 8c, dashed red and blue curves) are well described by $t_{av} \sim 1/V^2$. The raw simulation results are also well described by this scaling. Fitting simulation results for the $n_f = 1 \rightarrow 3$ transition (blue points) and $n_f = 3 \rightarrow 5$ transition (red points) to a power law form respectively yields the exponents -2.2 ± 0.04 and -1.95 ± 0.06, consistent with a $t_{av} \sim 1/V^2$ dependence.

This power law arises from the spooling process and can be explained by a simple argument. We argue that fold nucleation should occur when the compressive force rises to a critical value f_* sufficient to drop the free energy barrier to $\sim k_BT$. The time t_{av} will then be determined by the time required for f_c, given by eq 14, to rise to f_*. We can directly compute this time for the $n_f = 1 \rightarrow 3$ transition, using appropriate kinetic equations for dynamics of a single-fold eq 8. With $L_1 + L_2 = L$ in this case, combining eqs 8 and 14 give

$$f_c(t) = \gamma V(L/2)[1 - \exp(2t/\tau)] \tag{16}$$

so that $f_c(t_{av}) = f_*$ leads to

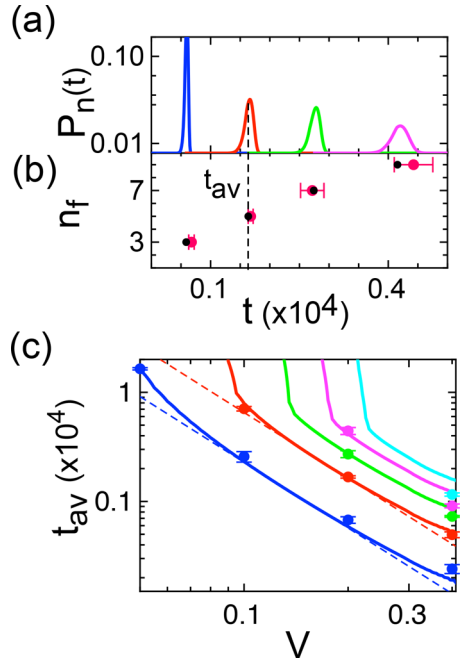

Figure 8. (a) Predicted nucleation time probability distributions for compression event with $D/P = 0.16$ ($\kappa = 120$) and $V = 0.2$. The blue curve gives distribution of times at which a single double-fold occurs or distribution of transition times to a state with $n_f = 3$. The red curve gives distribution of times at which a second double-fold occurs or distribution of transition times to a state with $n_f = 5$. The light green curve gives distribution of times at which a third double-fold occurs or distribution of transition times to a state with $n_f = 7$. The magenta curve gives distribution of transition times to a state with $n_f = 9$. (b) Resulting average folding times t_{av} for simulation and theory. (c) Average folding times obtained from simulation and theory as a function of V (data points simulation and bold curves theory; same color scheme with cyan giving average transition time to $n_f = 11$). Note that the best fit value of $\tau_0 = 0.32$. The blue and red dashed curves respectively give fits of simulation output to the power-law model $t_{av} \sim 1/V^2$ for the $n_f = 3$ and $n_f = 5$ transition time curves. The folding times are all shown in snapshot units relative to average time at which a single-fold occurs (i.e., average transition time to $n_f = 1$).

$$t_{av} = \frac{L}{4V}\log\left[\frac{1}{1 - \left(\frac{2}{L}\right)\frac{f_*}{\gamma V}}\right] \approx \frac{f_*}{2\gamma}\frac{1}{V^2} \tag{17}$$

with the approximation holding in the limit that V is larger than $V_* \equiv (2/L)(f^*/\gamma)$. Thus, we recover a $1/V^2$ scaling. For a higher order transitions, we can no longer assume $L_1 + L_2 = L$. However, for short times following the transition, contour spooling from L_1 is transferred primarily to L_2, so that $L_1(t) + L_2(t) \approx L_1(0)$, and the same argument holds replacing L by $L_1(0)$. The detailed theory deviates from the power law at high V (Figure 8c, compare red and blue to dashed red and blue curves) due to the effect of the hinge correction on the compressive force (e.g., see discussion in the Supporting Information).

Finally, we note that the dynamic compressive force eq 14 can explain why, for high stiffness (Figures 1l and 3a–c), the folds are always nucleated at the fold position furthest from the piston (s_1). While the compressive force will only be nonzero when L_2 is nonzero, a large L_1 will increase this force, as it confers a higher spooling speed eq 14. Applying this argument to other fold positions $s_i > s_1$, we observe that L_1 is longer than

DOI: 10.1021/acs.macromol.7b02748
Macromolecules 2018, 51, 4012–4022

the other strands, so we expect the compressive force to be highest at the fold position s_1 and therefore the nucleation barrier is lowest at s_1.

CONCLUSION AND DISCUSSION

We will conclude with a discussion of what physical channel dimensions might be required to observe ordered nested folding dynamics for an experiment involving DNA compression in nanochannels. Experiments in this regime could almost certainly not be conducted with the original nanodozers assay due to the very low trap stiffness arising from the small beads needed to form the traps, but compressive hydrodynamic flow and electrophoresis could be used instead. As noted, in the frame moving with the gasket, the compression process in a nanodozer assay corresponds to compression against a gasket in uniform flow, so we do not expect the use of flow based forcing in experiments to give rise to fundamental differences in the response vis-à-vis the translating piston implementation. A nonuniform Poiseuille profile, for example, generated by pressure-driven flow would simply lead to an effective V determined by averaging the parabolic flow across the transverse DNA concentration profile.[42] In agreement with this expectation, recent experiments probing compression of chains using pressure-actuated hydrodynamics in large nanochannels (~300 × 400 nm) report the same scaling behavior as the original piston-based nanodozer experiments.[43]

The persistence length of DNA in the buffer conditions used in typical experiments is around 55 nm for a 10 mM tris-HCl buffer using an estimate based on Odijk−Skolnick−Fixman (OSF) theory.[44] The compression events with D/P = 0.48,0.32 then correspond respectively to channels 18 and 28 nm in dimension. Channels of this size can be made via conventional electron beam lithography using standard resists (although 18 nm does lie at the limits of what is possible without extensive process characterization). While the D/P = 0.48 results are not completely ordered, a nested-folding structure is apparent (Figure 3e).

The challenge in working with such small channels does not actually lie in developing novel fabrication processes (channels of this size can be made via conventional processes[5]), but in overcoming the high free energy barrier to drive DNA into the channels. For such small channels there is also a high probability of introducing defects in the fabrication process (e.g., which prevent DNA translocation down the channel). The entrance challenge has been addressed for sub-30 nm channels via a new top-loading technique based on variation of vertical confinement.[45] The problems with defects is also naturally addressed via top loading, as a molecule does not need to continuously traverse the entire channel extent to be loaded from above. Three-dimensional sculpting of a nanochannel inlet to produce continuously varying funnels is also an effective way to decrease the entrance barrier,[15] although it has not yet been demonstrated for sub-persistence length structures. Lastly, there are experimental approaches for increasing the persistence length, so that the nested dynamics can be observed for larger channel dimensions. One possibility is to work at low ionic strength buffer. For example, OSF theory predicts P rises to 82 nm at 1 mM and 115 nm at 0.5 mM; for these dimensions the D/P = 0.48 and 0.32 results correspond to channels of D = 39 and 55 nm. While experiments are more challenging at such low ionic strengths due to decreased DNA stability, DNA extension has been measured in nanochannels for sub-millimolar ionic strengths that drive the system into an Odijk regime.[46] Finally, proteins like recA can increase the DNA persistence length and lead to Odijk type behavior in larger nanochannels.[47]

Lastly, we believe that dynamic compression in the sub-persistence length regime is a rich system for further simulation and theoretical study. One fascinating problem is the formation of knots under compression; knotting has been observed to occur in DNA following compression in 60 nm channels,[48] yet there is no understanding of the detailed mechanism of how compression enhances knot formation. Another fascinating question is whether jamming[10,11] might be present and would be observed for a different combination of stiffness and velocity. Our system somewhat resembles phase transitions and self-organization in a driven lattice gas[49,50] where a first-order line joins a second-order line. However, the nature of the phase transition appears to be very different due to chain connectivity and confinement. Possibly the phase diagram of this soft matter system in the $\kappa-V$ plane can be mapped onto other models of dynamical phase transitions.

ASSOCIATED CONTENT

Supporting Information

The Supporting Information is available free of charge on the ACS Publications website at DOI: 10.1021/acs.macromol.7b02748.

Parametrization of hinge state and compressive force on hinge; Figures S1−S3 (PDF)

AUTHOR INFORMATION

Corresponding Authors

*E-mail: reisner@physics.mcgill.ca (W.R.).
*E-mail: Aniket.Bhattacharya@ucf.edu (A.B.).

ORCID

Walter Reisner: 0000-0003-3223-615X

Notes

The authors declare no competing financial interest.

ACKNOWLEDGMENTS

This work was funded through the Natural Sciences and Engineering Research Council of Canada (NSERC) Discovery Grants Program (Grant No. RGPIN 386212) and the Fonds de recherche du Quebec Nature et technologies (FQRNT) Projet d'equipe (PR-180418).

REFERENCES

(1) Petrov, A. S.; Harvey, S. C. Packaging Double-Helical DNA into Viral Capsids: Structures, Forces, and Energetics. *Biophys. J.* **2008**, *95*, 497.

(2) Marenduzzo, D.; Micheletti, C.; Orlandini, E. Biopolymer organization upon confinement. *J. Phys.: Condens. Matter* **2010**, *22*, 283102.

(3) Mikkelsen, M. B.; Reisner, W.; Flyvbjerg, H.; Kristensen, A. Pressure-Driven DNA in Nanogroove Arrays: Complex Dynamics Leads to Length- and Topology-Dependent Separation. *Nano Lett.* **2011**, *11*, 1598.

(4) Vestergaard, C. L.; Mikkelsen, M. B.; Reisner, W.; Kristensen, A.; Flyvbjerg, H. Transition state theory demonstrated at the micron scale with out-of-equilibrium transport in a confined environment. *Nat. Commun.* **2016**, *7*, 10227.

(5) Reisner, W.; Pedersen, J. N.; Austin, R. H. DNA Confinement in Nanochannels: Physics and Biological Applications. *Rep. Prog. Phys.* **2012**, *75*, 106601.

DOI: 10.1021/acs.macromol.7b02748
Macromolecules 2018, 51, 4012−4022

(6) Khorshid, A.; Zimny, P.; Tétreault-La Roche, D.; Massarelli, G.; Sakaue, T.; Reisner, W. Dynamic Compression of Single Nanochannel Confined DNA via a Nanodozer Assay. *Phys. Rev. Lett.* **2014**, *113*, 268104.
(7) Khorshid, A.; Amin, S.; Zhang, Z.; Sakaue, T.; Reisner, W. Non-Equilibrium Dynamics of Nanochannel Confined DNA. *Macromolecules* **2016**, *49*, 1933.
(8) Sakaue, T. Semiflexible Polymer Confined in Closed Spaces. *Macromolecules* **2007**, *40*, 5206.
(9) Jun, S.; Thirumalai, D.; Ha, B.-Y. Compression and stretching of a self-avoiding chain in cylindrical nanopores. *Phys. Rev. Lett.* **2008**, *101*, 138101.
(10) Berndsen, Z. T.; Keller, N.; Grimes, S.; Jardine, P. J.; Smith, D. E. Nonequilibrium dynamics and ultraslow relaxation of confined DNA during viral packaging. *Proc. Natl. Acad. Sci. U. S. A.* **2014**, *111*, 8345.
(11) Keller, N.; Grimes, S.; Jardine, P. J.; Smith, D. E. Single DNA molecule jamming and history-dependent dynamics during motor-driven viral packaging. *Nat. Phys.* **2016**, *12*, 757.
(12) Schnurr, B.; MacKintosh, F. C.; Williams, D. R. M. Dynamical intermediates in the collapse of semiflexible polymers in poor solvents. *Europhys. Lett.* **2000**, *51*, 279.
(13) Sakaue, E.; Yoshikawa, K. Folding and unfolding kinetics on a semiflexible polymer chain. *J. Chem. Phys.* **2002**, *117*, 6323.
(14) Lam, T. E.; Hastie, A.; Lin, C.; Ehrlich, D.; Das, S. K.; Austin, M. D.; Deshpande, P.; Cao, H.; Nagarajan, N.; Xiao, M.; Kwok, P.-Y. Genome Mapping on Nanochannel Arrays for Structural Variation Analysis and Sequence Assembly. *Nat. Biotechnol.* **2012**, *30*, 771.
(15) Zhou, J.; Wang, Y.; Menard, L. D.; Panyukov, S.; Rubinstein, M.; Ramsey, J. M. Enhanced nanochannel translocation and localization of genomic DNA molecules using three-dimensional nanofunnels. *Nat. Commun.* **2017**, *8*, 807.
(16) Huang, A.; Reisner, W.; Bhattacharya, A. Dynamics of DNA Squeezed Inside a Nanochannel via a Sliding Gasket. *Polymers* **2016**, *8*, 352.
(17) Hayase, Y.; Sakaue, T.; Nakanishi, H. Compressive response and helix formation of a semiflexible polymer confined in a nanochannel. *Phys. Rev. E: Stat. Phys., Plasmas, Fluids, Relat. Interdiscip. Top.* **2017**, *95*, 052502.
(18) Williams, D. R. M.; Warner, M. Statics and Dynamics of Hairpins in Worm-like Main Chain Nematic Polymer Liquid-Crystals. *J. Phys. (Paris)* **1990**, *51*, 317.
(19) Muralidhar, A.; Tree, D. R.; Dorfman, K. D. Backfolding of Wormlike Chains Confined in Nanochannels. *Macromolecules* **2014**, *47*, 8446.
(20) Dai, L.; Ng, S. Y.; Doyle, P. S.; van der Maarel, J. R. C. Conformation Model of a Back-Folding and Looping of a Single DNA Molecule Confined Inside a Nanochannel. *ACS Macro Lett.* **2012**, *1*, 1046.
(21) Cohen, A. E. Force-Extension Curve of a Polymer in a High-Frequency Electric Field. *Phys. Rev. Lett.* **2003**, *91*, 235506.
(22) Sevick, E. M.; Williams, D. R. M. Long-lived states in electrophoresis: collision of a polymer chain with two ore more obstacles. *Eur. Phys. Lett.* **2001**, *56*, 529.
(23) Sevick, E. M.; Williams, D. R. M. Collision of a field-driven polymer with a post: electrophoresis in microlithographic arrays. *Phys. Rev. Lett.* **1996**, *76*, 2595.
(24) Saville, P. M.; Sevick, E. M. Collision of a field-driven polymer with a finite-sized obstacle: A Brownian dynamics simulation. *Macromolecules* **1999**, *32*, 892.
(25) Hinch, E. J. Uncoiling a polymer molecule in a strong extensional flow. *J. Non-Newtonian Fluid Mech.* **1994**, *54*, 209.
(26) Smith, D. E.; Chu, S. Response of Flexible Polymers to a Sudden Elongational Flow. *Science* **1998**, *281*, 1335.
(27) Levy, S. L.; Mannion, J. T.; Cheng, J.; Reccius, C. H.; Craighead, H. G. Entropic Unfolding of DNA Molecules in Nanofluidic Channels. *Nano Lett.* **2008**, *8*, 3839.
(28) Grest, G. S.; Kremer, K. Molecular dynamics simulation for polymers in the presence of a heat bath. *Phys. Rev. A: At., Mol., Opt. Phys.* **1986**, *33*, 3628.
(29) Sokal, A. D. In *Monte Carlo and Molecular Dynamics Simulations in Polymer Science*; Binder, K., Ed.; Oxford University Press: New York, 1995; Chapter 2.
(30) Huang, A.; Adhikari, R.; Bhattacharya, A.; Binder, K. Universal monomer dynamics of a two-dimensional semi-flexible chain. *Europhys. Lett.* **2014**, *105*, 18002.
(31) Huang, A.; Bhattacharya, A. DNA confined in a two-dimensional strip geometry. *Europhys. Lett.* **2014**, *106*, 18004.
(32) Huang, A.; Bhattacharya, A.; Binder, K. Conformations, transverse fluctuations, and crossover dynamics of a semi-flexible chain in two dimensions. *J. Chem. Phys.* **2014**, *140*, 214902.
(33) Huang, A.; Hsu, H.-P.; Bhattacharya, A.; Binder, K. Semiflexible macromolecules in quasi-one-dimensional confinement: Discrete versus continuous bond angles. *J. Chem. Phys.* **2015**, *143*, 243102.
(34) Odijk, T. On the Statistics and Dynamics of Confined or Entangled Stiff Polymers. *Macromolecules* **1983**, *16*, 1340.
(35) Landau, L. D.; Lifshitz, E. M. *Statistical Physics*; Pergamon Press.
(36) Tree, D. R.; Wang, Y.; Dorfman, K. D. Mobility of a Semiflexible Chain Confined in a Nanochannel. *Phys. Rev. Lett.* **2012**, *108*, 228105.
(37) Matthews, R.; Louis, A. A.; Yeomans, J. M. Effect of topology on dynamics of knots in polymers. *EPL* **2010**, *89*, 20001−p1.
(38) van Gunsteren, W. F.; Berendsen, H. J. C. Algorithms for Brownian dynamics. *Mol. Phys.* **1982**, *45*, 637.
(39) Odijk, T. DNA confined in nanochannels: Hairpin tightening by entropic depletion. *J. Chem. Phys.* **2006**, *125*, 204904.
(40) Chen, J. Z. Y. Conformational Properties of a Back-Folding Wormlike Chain Confined in a Cylindrical Tube. *Phys. Rev. Lett.* **2017**, *118*, 247802.
(41) Reifenberger, J. G.; Cao, H.; Dorfman, K. D. Odijk Excluded Volume Interactions during the Unfolding of DNA Confined in a Nanochannel. *Macromolecules* **2018**, *51*, 1172.
(42) Stein, D.; van der Heyden, H. J.; Koopmans, W. J. A.; Dekker, C. Pressure-Driven Transport of Confined DNA Polymers in Fluidic Channels. *Proc. Natl. Acad. Sci. U. S. A.* **2006**, *103*, 15853.
(43) Amin, S.; Khorshid, A.; Zeng, L.; Zimny, P.; Reisner, W. A Nanofluidic Knot Factory based on Compression of Single DNA in Nanochannels. *Nat. Commun.* **2018**, *9*, 1506.
(44) Klotz, A. R.; Duong, L.; Mamaev, M.; de Haan, H. W.; Chen, J. Z. Y.; Reisner, W. Measuring the Confinement Free Energy and Effective Width of Single Polymer Chains via Single-Molecule Tetris. *Macromolecules* **2015**, *48*, 5028.
(45) Berard, D. J.; Michaud, F.; Mahshid, S.; Ahamed, M. J.; McFaul, C. M. J.; Leith, J. S.; Bérubé, P.; Sladek, R.; Reisner, W.; Leslie, S. R. *Proc. Natl. Acad. Sci. U. S. A.* **2014**, *111*, 13295.
(46) Kim, Y.; Kim, K. S.; Kounovsky, K. L.; Chang, R.; Jung, G. Y.; de Pablo, J. J.; Jo, K.; Schwartz, D. C. Nanochannel confinement: DNA stretch approaching full contour length. *Lab Chip* **2011**, *11*, 1721.
(47) Frykholm, K.; Alizadehheidari, M.; Fritzsche, J.; Wigenius, J.; Modesti, M.; Persson, F.; Westerlund, F. Probing Physical Properties of a DNA-Protein Complex Using Nanofluidic Channels. *Small* **2014**, *10*, 884.
(48) Metzler, R.; Reisner, W.; Riehn, R.; Austin, A.; Tegenfeldt, J. O.; Sokolov, I. M. Diffusion mechanisms of localised knots along a polymer. *Euro. Phys. Lett.* **2006**, *76*, 696.
(49) Leung, K.-t.; Schmittmann, B.; Zia, R. K. P. Phase Transitions in a Driven Lattice Gas with Repulsive Interactions. *Phys. Rev. Lett.* **1989**, *62*, 1772.
(50) Krug, J. Boundary-Induced Phase Transitions in Driven Diffusive Systems. *Phys. Rev. Lett.* **1991**, *67*, 1882.

DOI: 10.1021/acs.macromol.7b02748
Macromolecules 2018, 51, 4012−4022